applied sciences

MDPI

Article

Improving the Understanding of Landslide Development in Alpine Forest Regions Using the InSAR Technique: A Case Study in Xiaojin County China

Shu Zhou [1], Zhen Guo [1,2,*], Gang Huang [3] and Kanglin Liu [3]

[1] Department of Geotechnical Engineering, College of Civil Engineering, Tongji University, Shanghai 200092, China; shuzhou@tongji.edu.cn
[2] Key Laboratory of Geotechnical and Underground Engineering of the Ministry of Education, Tongji University, Shanghai 200092, China
[3] Sichuan Huadi Construction Engineering Co., Ltd., Chengdu 610081, China; hg1954@163.com (G.H.); 13880050194@163.com (K.L.)
* Correspondence: zhenguo@tongji.edu.cn

Abstract: Employing a small baseline subset Interferometric Synthetic Aperture Radar (SBAS-InSAR) and hotspot analysis, this study identified 81 potential landslides in a 768.7 km^2 area of Xiaojin county, eastern Tibetan Plateau. Subsequent time-series deformation analysis revealed that these potential landslides are in the secondary creep stage. The newly identified landslides were compared to a landslide inventory (LI), established through field surveying, in terms of causative factors, including altitude, slope, relief amplitude, distance to river, distance to road, and slope curvature. From the comparison, the InSAR technique showed the following advantages: (1) it identified 25 potential landslides at high altitudes (>3415 m) in addition to the low-altitude landslides identified through the field survey. (2) It obtained approximately 37.5% and 70% increases in the number of potential landslides in the slope angle ranges of 20°–30° and 30°–40°, respectively. (3) It revealed significant increases in potential landslides in every relief amplitude bin, especially in the range from 58 m to 92 m. (4) It can highlight key geological factors controlling landslides, i.e., the stratigraphic occurrence and key joints as the InSAR technique is a powerful tool for identifying landslides in all dip directions. (5) It reveals the dominant failure modes, such as sliding along the soil–rock interface and/or interfaces formed by complicated combinations of discontinuities. This work presents the significant potential of InSAR techniques in gaining deeper knowledge on landslide development in alpine forest regions.

Keywords: alpine forest region; InSAR; landslide inventory; hotspot analysis

check for updates

Citation: Zhou, S.; Guo, Z.; Huang, G.; Liu, K. Improving the Understanding of Landslide Development in Alpine Forest Regions Using the InSAR Technique: A Case Study in Xiaojin County China. *Appl. Sci.* **2023**, *13*, 11851. https://doi.org/10.3390/app132111851

Academic Editor: Gaetano Zizzo

Received: 26 August 2023
Revised: 6 October 2023
Accepted: 13 October 2023
Published: 30 October 2023

Copyright: © 2023 by the authors. Licensee MDPI, Basel, Switzerland. This article is an open access article distributed under the terms and conditions of the Creative Commons Attribution (CC BY) license (https://creativecommons.org/licenses/by/4.0/).

1. Introduction

Landslides are a type of earth-surface mass wasting driven by the force of gravity [1]. In alpine forest regions, the distribution and development of landslides are related to various factors, such as regional topographic conditions, geological settings, and human activities [2,3]. In terms of topographic conditions, slope relief controls the gravitational potential energy of slope masses, indicating the ability of landslide formation [4]. Slope degree influences the free surface of slopes, which is associated with slope displacement [5]. Geological conditions including slope material properties and tectonic development are considered as internal controlling factors for landslide formation [6]. Slope material properties, such as rock or soil type, thickness, and strength, determine the possibility of a slope evolving into a landslide [7,8]. Regional tectonics including earthquakes and active faults contribute to landslide development over long time periods by weakening the strata and initiating dynamic loadings on slopes [9]. Human activities introduce some changes in the geological and topographic conditions of the slope and, thus, accelerate the development

of landslides [10–12]. Understanding the relationship between landslides and the above-mentioned factors is, thus, crucial for determining the regional development of landslides and taking apposite measures to mitigate and prevent landslide hazards.

Many studies investigated factors affecting landslide development through various means, such as physical tests [13–16], numerical simulations [17–19], and statistical methods [20,21]. At present, the most effective method has not yet been established because the characteristics of landslides and influencing factors vary from region to region. Nevertheless, statistical methods are considered feasible at the regional scale. This is because (1) physical model-based methods are more applicable to the study of individual landslides, (2) numerical simulation-based methods demand high computational costs, and (3) both physical and numerical modeling require high-resolution updating of geological structures and environmental conditions, which are difficult to implement at the regional scale.

Building an accurate, up-to-date, and complete landslide inventory is a prerequisite for landslide development analysis at the regional scale using statistical methods [20]. However, compared to relatively low-altitude areas, an alpine forest region is characterized by complex topography, high altitude, steep terrain, and high climate sensitivity [22]. These specific features pose challenges to the construction of a complete landslide inventory. Traditionally, landslides in alpine forest regions are usually identified through morphological evidence such as cracks, collapse, and ground deformation [23]. Such evidence of landslides might be hidden or nonvisible in the early stage of landslide evolution [24]. For example, if a landslide area is densely vegetated, cracks and deformation are difficult to observe [25]. For slow-moving landslides, morphological evidence may not be sufficiently distinct [26]. Further, the terrain condition in alpine forest regions may also limit the identification of landslides in field geological surveys [27]. Specifically, ridge-top landslides in alpine forest regions are often located at the top of mountains with high relief and no road access and are barely detectable [28]. For instance, the Maoxian landslide in southwest China, which was a massive landslide with a volume of approximately 1.8×10^7 m^3 (Chinese Government, 2017) that eventually claimed 83 lives [29,30], was not identified through a field survey because the sliding body was located at the inaccessible top of the Fugui Mountain [31]. In addition, the development of landslides is a dynamic process that can be triggered by many external factors such as earthquakes and intense rainfall [32]. If the field survey is conducted with long time intervals, new landslides would not be detected.

The development of Synthetic Aperture Radar (SAR) technology has opened new opportunities for identifying potential landslides in alpine forest regions [33]. SAR satellites have various advantages, such as being able to penetrate vegetation, continuously observe the earth surface with all-day and all-weather capability, and collect high-resolution SAR images with a short time interval [34]. With continuous SAR images, Interferometric SAR (InSAR) techniques, including Differential InSAR (D-InSAR) [35,36], Permanent Scatterer (PS) InSAR [37,38], and Small Baselines Subset (SBAS) InSAR [39,40], can be applied to analyze ground deformation and identify potential landslides with high precision, especially in alpine forest regions [41,42]. For example, Bianchini et al. [43] identified 1012 active landslides and 64 new potential landslides within an area of 4470 km^2 in the Calabria region, south Italy, using ENVISAT data. Zhang et al. [28] performed SBAS-InSAR analysis on 40 scenes of Sentinel-1 SAR data and identified 72 active landslides in Wenchuan, China. The InSAR technique has proved to be a powerful tool for landslide studies [44,45]. However, previous studies mainly focused on landslide deformation analysis [46,47], potential landslide detection [48,49], and improving the InSAR method [50]. Only a few studies have discussed the role of the InSAR technique in understanding the development of potential landslides at the regional scale.

In summary, as SAR satellites support continuous observation of an area and can detect ground deformation with high precision, InSAR analyses would contribute to the construction of a complete regional landslide inventory and, therefore, provide an opportunity to improve the understanding of landslide development at the regional scale, especially in alpine forest regions. Accordingly, this study performed SBAS-InSAR analysis and

hotspot analysis in an attempt to build a new landslide inventory for Xiaojin county, which is a typical alpine forest region in western Sichuan Province, China. The new landslide inventory was then compared with a landslide inventory built using field survey data to explore the effectiveness of the InSAR technique in understanding landslide development.

2. Study Area

The study area (102.20° E–102.51° E, 30.87° N–31.12° N) is located in Xiaojin County, Sichuan province, Southwest China (Figure 1). The terrain is extremely complicated, with a high mountain and canyon landform that formed under the influence of strong Himalayan tectonic movements and surficial erosion. The canyons are mainly distributed along rivers, with an altitude below 3500 m. In contrast, the altitude of the high mountains ranges from 3500 m to about 5000 m. Forests in Xiaojin county are well developed, with a total forest area accounting for 58.8% of the county's total area. Regarding the weather conditions in the study area, the area is located in the plateau monsoon climate zone according to the geomorphological division of China [51–53]. According to the monthly average rainfall during 1981–2010 (Figure 2), the rainfall in this region mainly occurs during May–October, accounting for 84.2% of the annual precipitation, and the maximum average rainfall occurs in June (126.2 mm), accounting for 20.0% of the annual precipitation. The maximum hourly rainfall (28.4 mm) occurred on 8 June 1984. Under the abovementioned topographical, weathering and rainfall conditions, the concentrated rainfall in summer can saturate the soil on the slope and trigger frequent landslides.

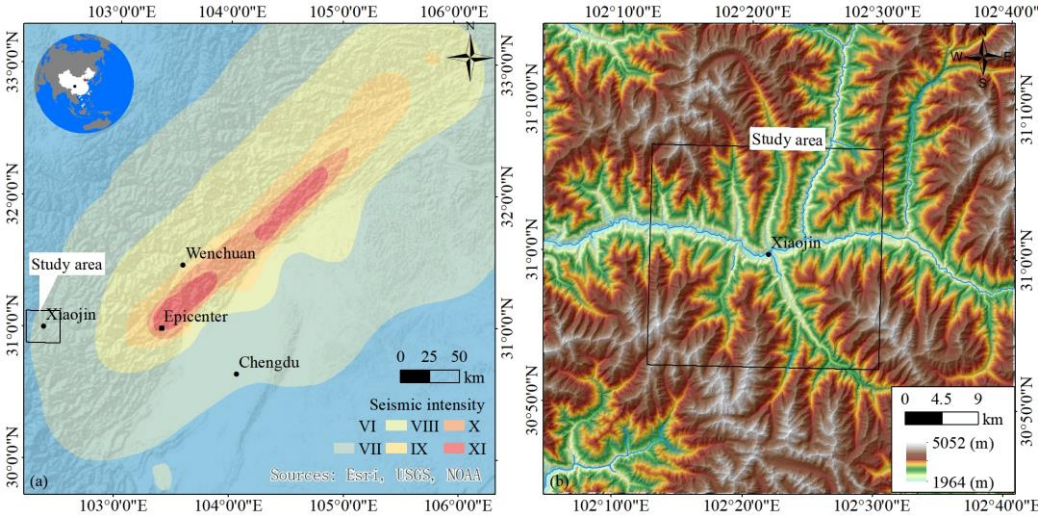


Figure 1. Location (**a**) and topography (**b**) of the study area. The background colors in (**a**) show the seismic intensity of the Wenchuan earthquake (Ms = 8.0) in 2008. The topographic data in (**b**) are from the Earth Science Data Systems (ESDS) Program of NASA.

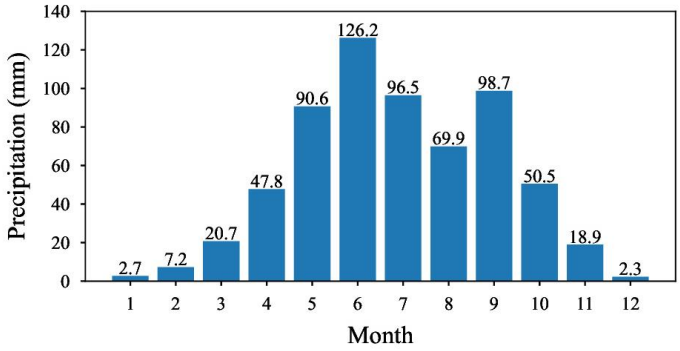


Figure 2. Monthly average precipitation in the study area in 1981–2010 (http://data.cma.cn/ (accessed on 12 October 2023)).

The geological map (Figure 3) shows that the geological setting in the study area is complicated due to the historical tectonic movements. During the late Indosinian Movement, the Proterozoic and Mesozoic strata underwent strong folding and metamorphism, forming a series of northwest-trending folds and metamorphic rocks. The regional faults are barely developed in the study area, while some small-scale faults trending northwest and northeast are sporadically distributed in the study area. There are two major groups of joints in the study area with average dip directions of 143° and 293° and dip angles of 76° and 82°, respectively. Rock outcrops in the study area are mainly Quaternary deposits (*Q*), the Zhuwo Formation of the upper Triassic system (T_3zh), and the Zagunao Formation of the middle Triassic system (T_3z) (Figure 3). They are characterized as follows:

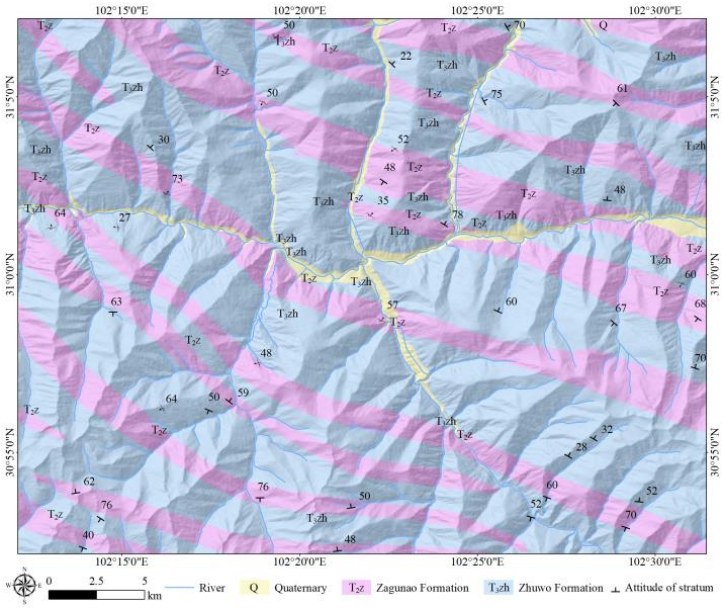


Figure 3. Geological map of the study area (based on the China Geological Survey at http://www.cgs.gov.cn/ (accessed on 12 October 2023)).

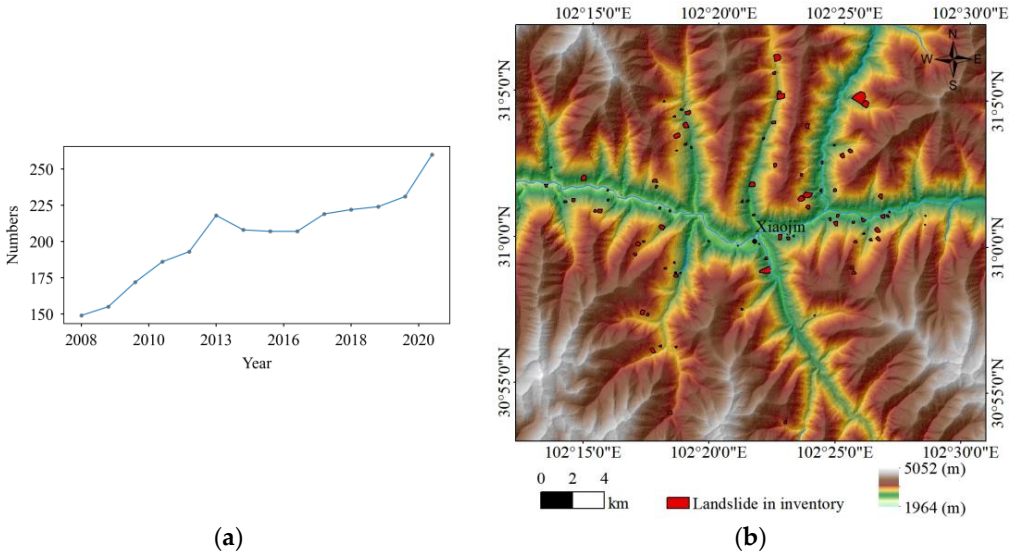
- The Quaternary deposits mainly consist of moraine debris, alluvium, proluvium, and eluvium. They are widely distributed in river valleys and high mountainous areas, reaching tens of meters in thickness and forming nearly vertical slopes on roads and residential areas.
- T_3zh consists mainly of fine-grained metamorphic sandstone, metamorphic silt, carbonaceous sericite slate, and silty slate. Its thickness ranges from 834 m to 1949 m regionally.
- T_3z is foliated metamorphic calcareous sandstone and feldspar quartz sandstone interbedded with dark grey slate.

According to the field investigation, the soil and rocks of these strata are usually vulnerable. Geotechnical tests show that the internal friction angle of the soils in some landslides was as low as 20.4° under unsaturated conditions and 17.8° under saturated conditions. The historical earthquake catalogue shows that, although the study area had not been struck by strong earthquakes directly, it is located in the impact range of several strong events (Table 1). For example, the study area was affected by the Wenchuan earthquake in 2008 (Ms 8.0 according to the Chinese Earthquake Administration) and the seismic intensity was approximately VII (Figure 1a). Frequent strong earthquakes around the Xiaojin area could weaken the rock mass, contributing to the formation of landslides.

Table 1. Historical earthquakes that impacted the study area (according to the Chinese Earthquake Administration).

Date	Epicenter Location	Magnitude	Distance to Study Area (km)
18 February 1991	Xiaojin county	5.0	60
12 May 2008	Wenchuan county	8.0	108
20 April 2013	Lushan county	7.0	109
22 November 2014	Kangding county	6.3	95

Landslide hazards in the study area are well developed. The historical landslide records of Xiaojin county show a rapid increase in the number of landslides after the Wenchuan earthquake in 2008, with an annual increment rate of about 8.5 (Figure 4a). By 2021, 260 landslides were identified in Xiaojin county, 93 of which were located in the study area. The spatial distribution of the landslides in the current landslide inventory established through the field survey (Figure 4b) shows that the landslides are mainly located in the valley along the river and most of them are distributed at relatively low altitude.



(**a**) (**b**)

Figure 4. Landslides in the Xiaojin area (data provided by the Department of Natural Resources of Sichuan province). (**a**) Accumulated number of landslides in Xiaojin area and (**b**) the spatial distribution of landslides in the study area determined through a field survey. Note that the accumulated number of landslides dropped in 2014 in (**a**) because some landslides were removed from the inventory as the long-term in situ monitoring indicated no further displacement.

3. Data and Methods

The workflow of this study is presented in Figure 5. In the InSAR analysis, the well-known open-source package InSAR Scientific Computing Environment version 2 (ISCE2 version v2.5.0, https://winsar.unavco.org/software/isce (accessed on 12 October 2023)) was used to generate a single interferogram and single look complex (SLC) stack. SBAS analysis was performed with the Stanford Method for Persistent Scatterers (StaMPS version 4.1b1, http://homepages.see.leeds.ac.uk/~earahoo/stamps/ (accessed on 12 October 2023)) software [54–56] to obtain the ground deformation rate, followed by spatial statistical analysis to determine potential landslides.

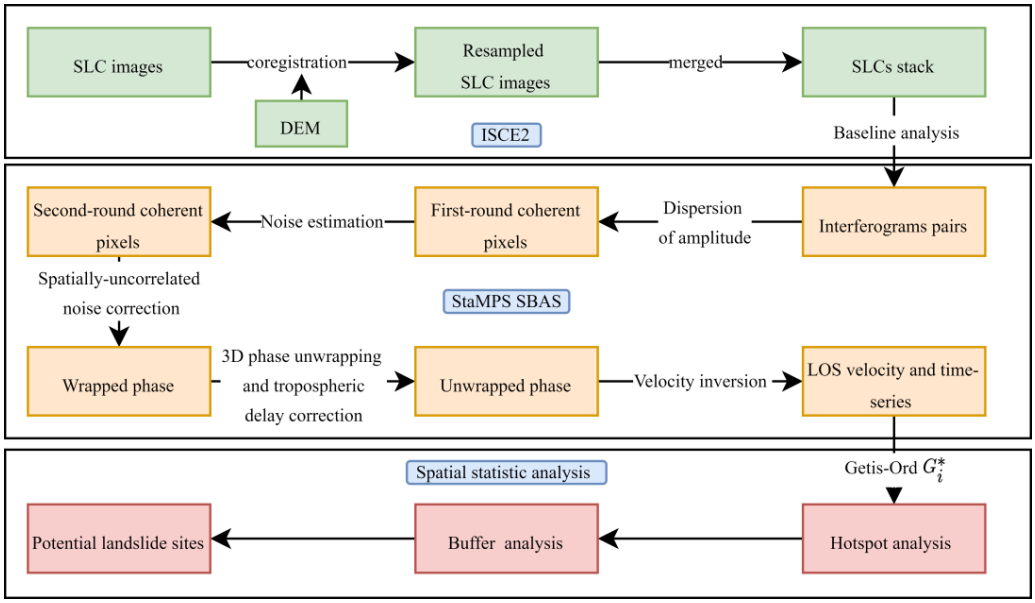


Figure 5. Workflow of the data processing in this study.

3.1. Data Sets

This study analyzed data sets from many sources. For the InSAR analysis, two Sentinel-1 data sets with range and azimuth resolutions of 2.3 m and 14 m, respectively, were acquired from the European Space Agency (ESA). The detailed information of the used Sentinel-1 images is presented in Table S2 and the spatial coverage of SLCs and the geometric relationship between the SLCs and the study area are shown in Figure S1. It is noteworthy that the combination of ascending and descending data can reduce the slope effects on the observed geometry [57]. The STRMGL1 digital elevation model with a resolution of 30 m was downloaded from the Land Processes Distributed Active Archive Center (https://lpdaac.usgs.gov (accessed on 12 October 2023)) and used for co-registration and flat-earth phase removal in the single interferogram generation processes of SLCs. Gaofen-2 optical images with a resolution of 2 m were collected from the China Center for Resource Satellite Data and Applications (http://www.cresda.com/ (accessed on 12 October 2023)) to assist in the analysis of landslide spatial geometry. Unmanned aerial vehicle (UAV) images with a resolution of less than 0.2 m were used to determine the shape of landslides during the field investigation. The landslide inventory map provided by the Department of Natural Resource of Sichuan Province was used to analyze the spatial distribution characteristics.

3.2. Methods

3.2.1. Theory of SBAS-InSAR Analysis

The SBAS-InSAR method proposed by Berardino et al. [58] is a popular time-series InSAR method. It utilizes interferometric pairs of small time–space baselines to obtain ground deformation. The SBAS-InSAR technique can overcome the low coherence of interferograms induced by a single super-image and weaken the influence of the atmosphere and troposphere. With these advantages, the SBAS-InSAR technique is considered as an effective method for monitoring land deformation with sub-centimeter accuracy [39,50,59]. In this study, the SBAS-InSAR package of StaMPS was used. The detailed theory and workflows were referred from the literature [56,60,61].

3.2.2. Cluster Extraction with Spatial Statistical Analysis

After extracting ground deformation through the SBAS-InSAR analysis, potential landslides in the mountainous areas were identified by selecting ground deformation with a specific deformation rate threshold (DRT) [62]. This analysis is based on the assumption

that the deformation rate is higher in landslide-prone areas than in non-landslide areas [63]. However, considering the spatial variation in the geological conditions and the failure mechanism of landslides, the DRTs may vary among different regions and cannot be defined by a fixed rule. Nevertheless, the deformation of the landslide body is controlled by the failure mechanism and is continuously distributed in space but cut off at the landslide boundary [42]. This suggests that, from the spatial statistic viewpoint, the deformation would cluster in the landslide body. Therefore, the cluster analysis of the deformation rate obtained from the InSAR technique can be used to determine potential landslide sites. Compared with the DRT method, the cluster analysis is considered to be a more effective and general tool for determining landslide sites in mountainous areas. In this study, one of the famous cluster analysis methods, termed the hot spot analysis, was used to cluster the InSAR results and further determine potential landslide sites [64]. In the analysis, the G_i^* value, an indicator for potential landslide, is calculated as follows [65,66]:

$$G_i^* = \frac{\sum_{j=1}^{n} w_{i,j}x_j - \overline{X}\sum_{j=1}^{n} w_{i,j}}{S\sqrt{\frac{\left[n\sum_{j=1}^{n} w^2{}_{i,j} - \left(\sum_{j=1}^{n} w_{i,j}\right)^2\right]}{n-1}}} \quad (1)$$

where x_j is the deformation rate obtained by InSAR analysis; n is the number of the measured points; $w_{i,j}$ is the spatial weight of points i and j, which are used in statistics; and $\overline{X}$ and S are the mean and standard deviation of the deformation rate, respectively.

In the processes of calculating G_i^*, the z-score and p-value were also obtained. For a statistically significant positive z-score, the higher the z-score, the more concentrated the cluster (hot spot). For a statistically significant negative z-score, the lower the z-score, the more concentrated the cluster (cool spot). The critical values of the z-score at clustering confidence coefficients of 90%, 95%, and 99% were $\pm$1.65 (p-value = 0.10), $\pm$1.96 (p-value = 0.05), and $\pm$2.85 (p-value = 0.01), respectively [67]. In general, a higher confidence coefficient reflects a better clustering result. However, a higher confidence coefficient could also narrow down the landslide deformation area as well as ignore some small landslides. Thus, the critical z-score was set as $\pm$1.96 (95% confidence coefficient) to maximize the potential landslide detection in this study.

After the hot spot analysis, the clustered ground deformation velocity was obtained. However, some noised measure points (MPs) still appeared and obstructed the identification of potential landslide sites. To eliminate the noised MPs, buffer analysis was conducted following the procedure described by Meisina et al. [68]. In the analysis, a potential landslide area is determined by clusters with a minimum of three MPs and a maximum buffer size of 50 m for each MP [67,68]. However, considering the large distance between the MPs on the slope because of the large slope in the study area, the maximum buffer size was set to be 75 m through several runs of trial-and-error analysis.

4. Results

4.1. Ground Deformation

Ascending and descending data sets of Sentinel-1 SLCs were processed using the SBAS-InSAR technique. As the images have short spatial and temporal baselines, the SLCs exhibited good interferometric performance. In the determination of the subsets, images covering a period of 120 days with a spatial baseline less than 250 m were used to generate interferogram pairs for ascending orbit SLCs. The minimum temporal and spatial baselines for the SLCs in descending orbit were 150 days and 240 m, respectively. Meanwhile, to eliminate decorrelated pairs and ensure the absence of isolated clusters of images [54–56], a coherent threshold of 0.4 was set through a series of trial-and-error analyses. After the abovementioned selection, 457 and 487 pairs of SLCs were obtained for the ascending and descending orbit data sets, respectively, and the baseline connections are shown in Figure S2.

After the SBAS-InSAR analysis, the ground deformation velocities were obtained with respect to a reference point, where ground deformation is almost zero. The spatial distributions of the annual ground deformation velocities in LOS from the ascending and descending data sets are shown in Figures 6 and 7, respectively, and the reference points are marked as the red star. The ground deformation velocities have positive and negative values, which correspond to the ground moving towards and away from the satellite, respectively. For the ascending data set, a total of 21,613 MPs were generated with an average density of 45.6 MPs/km^2. For the descending data set, 19,507 MPs were obtained with an average density of 42.1 MPs/km^2. The density of MPs in alpine mountains is lower than that in valley areas, which may be attributed to the complicated terrain conditions and the dense vegetation coverage in alpine regions. The deformation velocities fall in the ranges of [−84.4, 21.9] mm/year and [−41.0, 17.8] mm/year in the ascending and descending data sets, respectively; they were mainly concentrated at ±5 mm/year for both data sets (yellow dots in Figures 6 and 7). The low deformation velocities indicate that most of the study area was relatively stable during the monitoring stage. The two data sets showing different extreme values might be attributed to two factors: (1) the two data sets have different geometric relationships with the study area and (2) the descending data set captures the minimum deformation velocity (−84.4 mm/year), whereas the ascending data set misses it due to the data coverage (area around TS1 in Figure 6). Focusing on areas with high deformation velocity (red and green clusters in Figures 6 and 7), they are characterized by strong spatial agglomeration and uneven distribution and mainly distributed in the 'V'-shape valley landforms along the rivers. Some of the high deformation areas are captured by both the ascending and descending data sets, such as the area around TS2, TS6, and TS7. However, some are detected by only one data set, such as TS3 in Figure 6 and TS4 in Figure 7. This difference might be explained by the different geometric relationships between the satellites' orbits and slope and indicates that the combination of both the ascending and descending data sets would improve the identification of more instances of ground deformation and, thus, provide an opportunity to better understand the development of regional landslides.

The time series of the displacement at nine sample MPs (TS1–TS9, see Figures 6 and 7 for their locations) were extracted and are plotted in Figure 8. The MPs of TS1–TS7 are located in the area with high deformation velocity, while the MPs of TS8 and TS9 are in the river valley where the deformation rate is relatively low. The deformation in the river valley obtained from the ascending data set fluctuates around 0 mm, indicating the absence of prominent ground movement (Figure 8a). The time series at TS2 (orange line in Figure 8a) shows that the deformation was approximately 0 mm before September 2020, but deformation tended to appear afterward. According to the definition of reactivated landslides, this deformation pattern accords with a reactivation phenomenon. The maximum annual deformation velocity in the study area appeared at TS1 and the accumulated deformation reached approximately 167.1 mm at the end of the observation period (Figure 8a). The deformations at MPs TS1, TS3, TS5, TS6, and TS7 increased linearly with time (Figure 8a), suggesting that these slopes are in the secondary creep stage and the index of instability is in a limit equilibrium stage [31]. According to the inverse-velocity failure model, these slopes are not expected to fail as long as there is no strong impact such as intense rainfall and earthquake [62,69]. The deformation time series at TS2, TS6, TS7, TS8, and TS9 obtained from the descending data set (Figure 8b) show similar trends as those from the ascending data set (Figure 8a). However, the displacement at TS2 before September 2020 fluctuated between 0 and −40 mm with the descending data set (Figure 8b) rather than around 0 mm with the ascending data set (Figure 8a). This might suggest the heterogeneous displacement on the slope as the MPs in different data sets are not located exactly at the same point because of the variable satellite–slope geometric relationships.

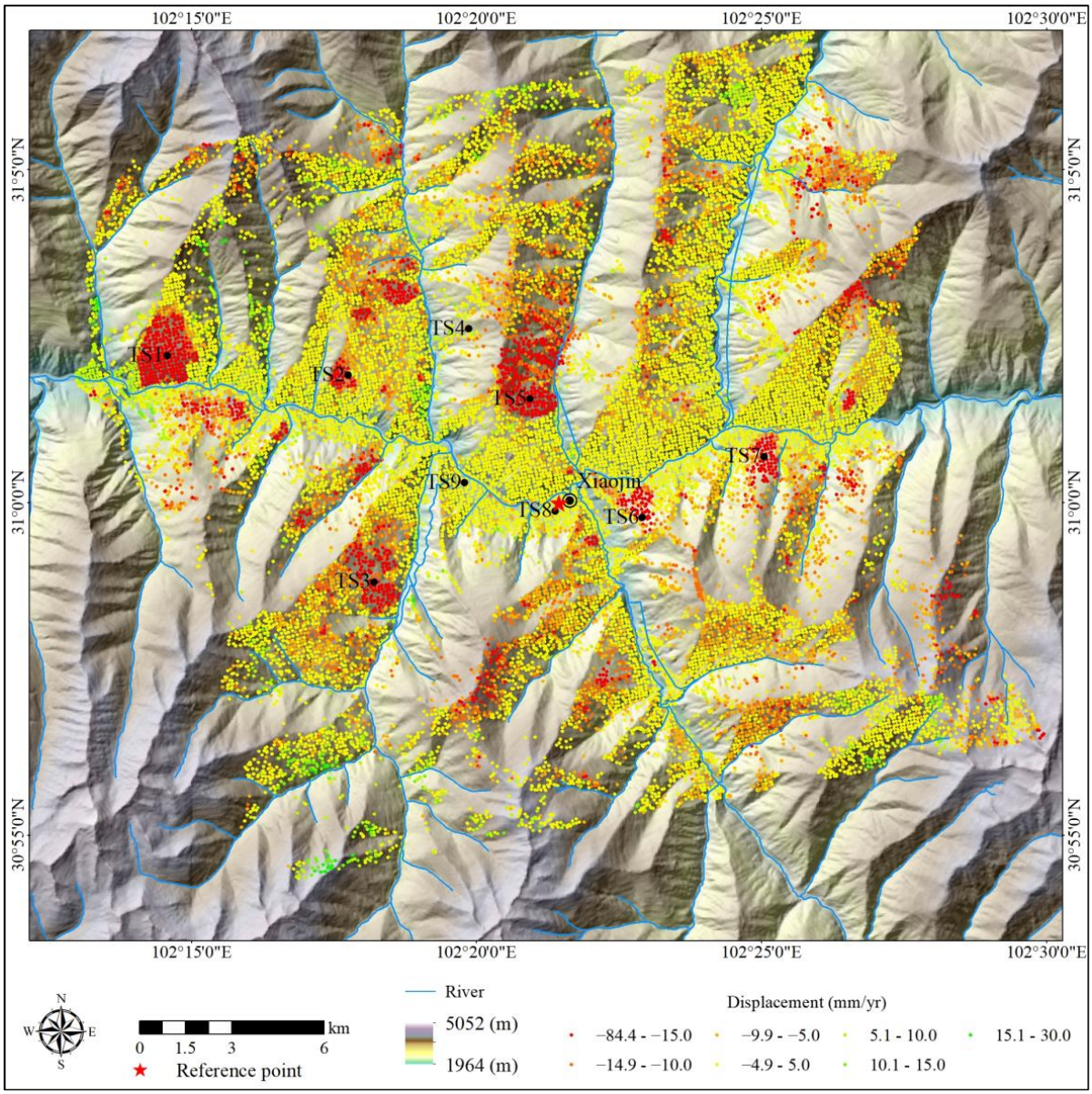


Figure 6. Ground deformation velocity along the LOS direction obtained from the ascending orbit SAR images.

4.2. Potential Landslides

Hot and cold spots were obtained through cluster analysis and 846 and 1024 MPs were clustered as hot or cold spots in the ascending and descending data sets, respectively. The hot spot maps (Figure 9) show that MPs with large deformation velocities were well extracted, and some areas that were difficult to be determined in the velocity map were well grouped through the hot spot analysis. For example, the deformation boundary at TS2 is fused and difficult to distinguish in the descending deformation map (Figure 7) because of the existence of two adjacent deformation areas on the slope. Nevertheless, it could be grouped into two different deformation areas after the cluster analysis (Figure 9b). This implies that the hot spot analysis is highly applicable for the potential landslide identification.

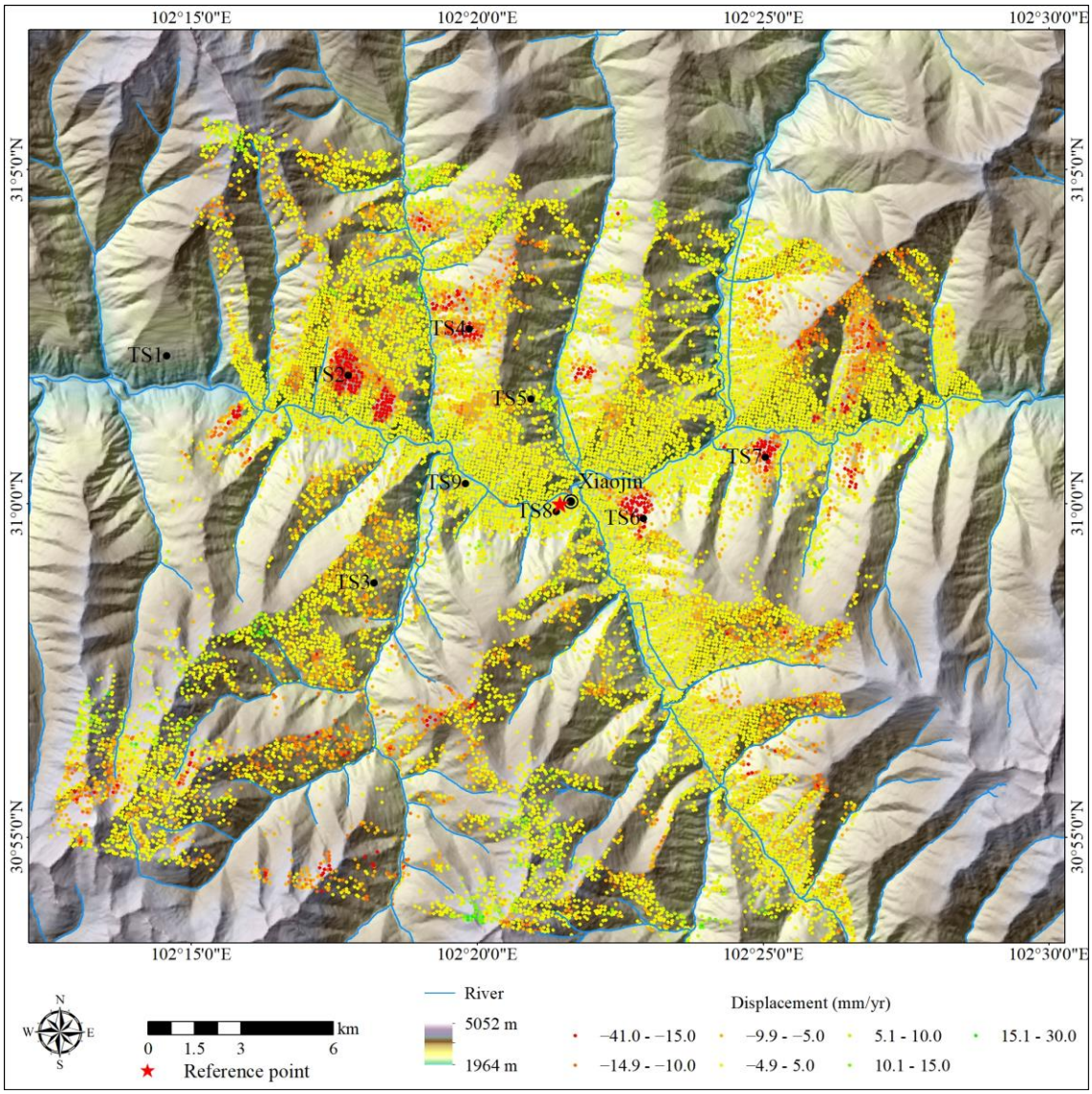


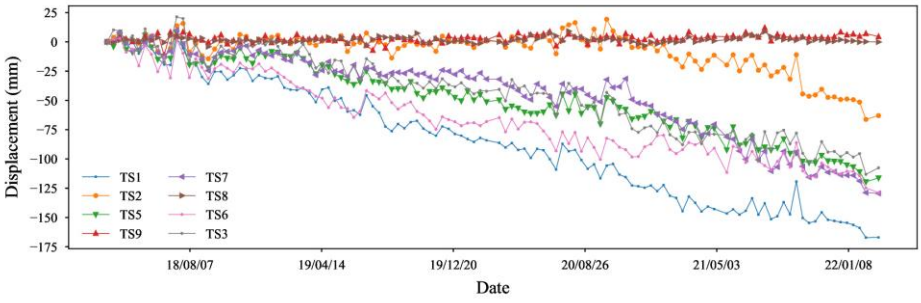
Figure 7. Ground deformation velocity along the LOS direction obtained from the descending orbit SAR images.

Figure 10 shows the potential landslides identified by the cluster and buffer analyses, combining the ascending and descending data sets. A total of 99 deformation patches with more than 3 MPs at each patch were obtained and the total, mean, and standard deviation of the patch areas were 15.68 km^2, 0.158 km^2, and 0.284 km^2, respectively. These patches were mainly distributed along the rivers, accounting for approximately 80% of the total deformation patches and the largest patch appeared at TS1 with an area of 2.24 km^2.

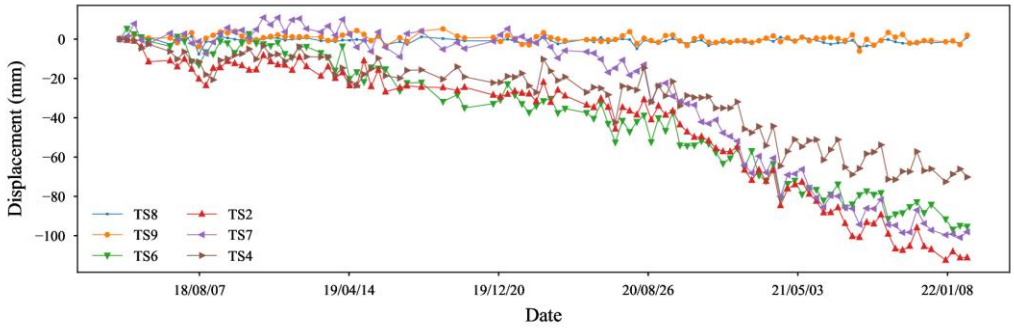
4.3. Potential Landslides Validation

The potential landslide sites identified through the InSAR analysis in this study were primarily verified against field investigation, and some inaccessible ridge-top sites were validated via optical image interpretation according to the procedure described in Zhou et al. [62] and topographic map analysis [64]. The UAV images and optical images in Figure 11 clearly show examples of the cracks and scars induced by slope sliding in the study area that were used to validate potential landslides. In particular, the Chunchangba site, located at TS6 (see Figure 6 for its location), was selected as a typical case to further highlight the validation. The SAR results show that the average annual deformation

velocity around Chunchangba site reached −28.85 mm/year in the ascending data set and −20.23 mm/year in the descending data set, indicating significant ground motion in the slope. The UAV photogrammetry showed the existence of large deformation as well as cracks and rockfalls on the slope (Figure 12). These results suggest that the InSAR results are accurate and the Chunchangba area is confirmed as an active landslide site. In summary, a total of 81 potential landslide sites were confirmed, accounting for 81.82% of the entire clustered results. The remaining sites were eliminated because they are mostly related to the activities of glacial till or superficial material movement (Figure 11d).



(**a**)



(**b**)

Figure 8. Time series of displacement at sample monitoring points (see Figures 6 and 7 for their locations) obtained from the ascending (**a**) and descending (**b**) data sets. Note: the initial displacement of each monitoring point is assumed to be 0 mm.

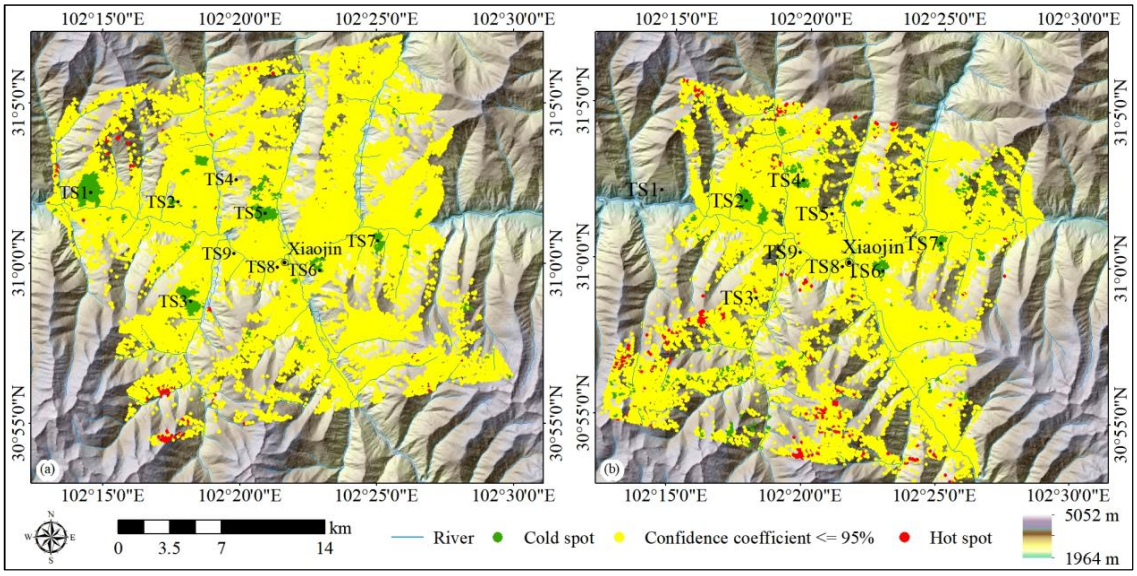


Figure 9. Results of hot spot analysis using the (**a**) ascending and (**b**) descending data sets.

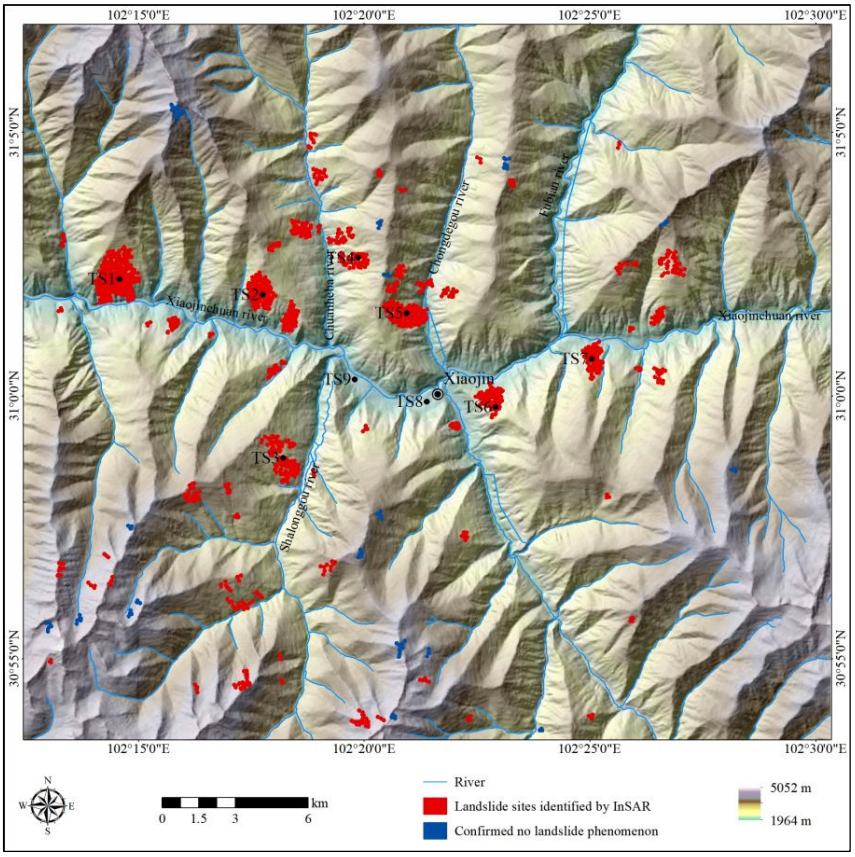


Figure 10. Potential landslide sites obtained through cluster and buffer analyses.

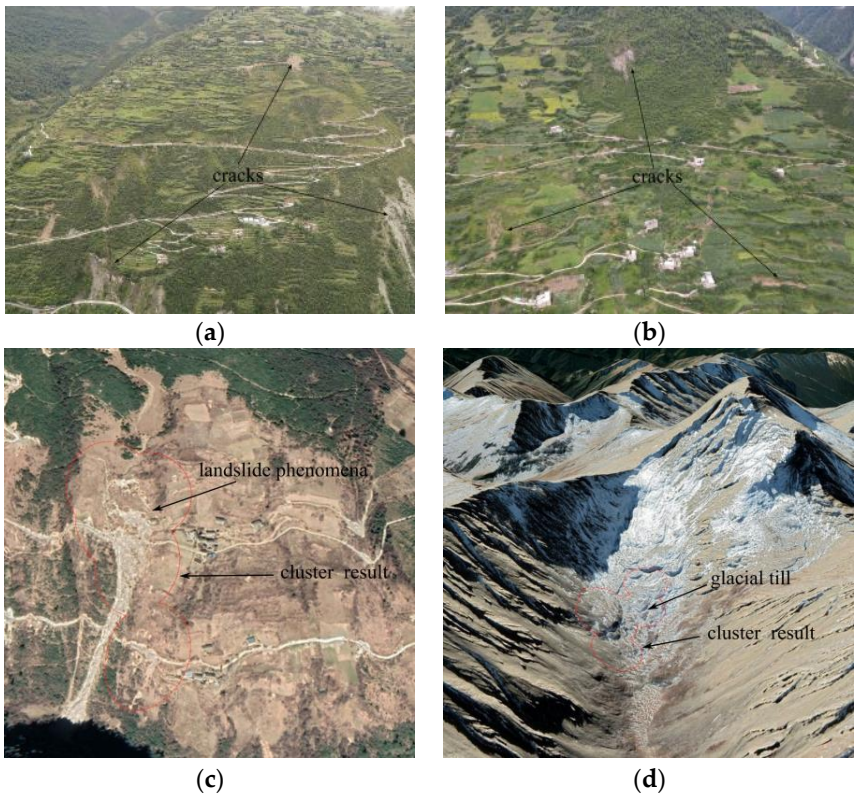


Figure 11. Deformation evidence in the study area from UAV images (**a**,**b**) and optical images (**c**,**d**).



Figure 12. UAV image showing the landslide phenomenon in the Chunchangba area.

5. Discussion

5.1. New Understanding of Landslide Development

Understanding the development of landslides is critical for landslide hazard assessment as well as risk management. The results have shown that the InSAR technique is applicable to the identification of new landslides on the regional scale and can enhance the existing landslide inventory. Moreover, it would be of scientific significance to clarify how the newly identified landslides improve the understanding of landslide development in alpine forest regions. For this purpose, the statistic characteristics of the newly identified landslides by the InSAR technique and the landslide inventory established by field survey were compared in terms of frequently used landslide causative factors, namely altitude, slope, relief amplitude, distance to river, distance to road, and curvature of slope [70]. The results of the comparison are shown in Figure 13.

As shown in Figure 13a, the landslides identified through field investigation are all distributed below the altitude of 3415 m. The InSAR technique not only reveals more landslides in almost all altitude groups than the field survey but also identifies 25 potential landslides at high altitudes (>3415 m), suggesting the advantage of the InSAR technique in detecting high-altitude landslides. A reasonable explanation for the difference is that landslides at high altitudes are difficult to identify through field investigations owing to the steep terrain and lack of road connectivity, while SAR satellites can easily capture high-altitude landslides with high accuracy. Recent studies support this explanation. For example, the Maoxian landslide and Baige landslide were missed in field investigations because they are located in a high-altitude region. However, they were clearly identified in post-analysis using InSAR techniques [31,71–73].

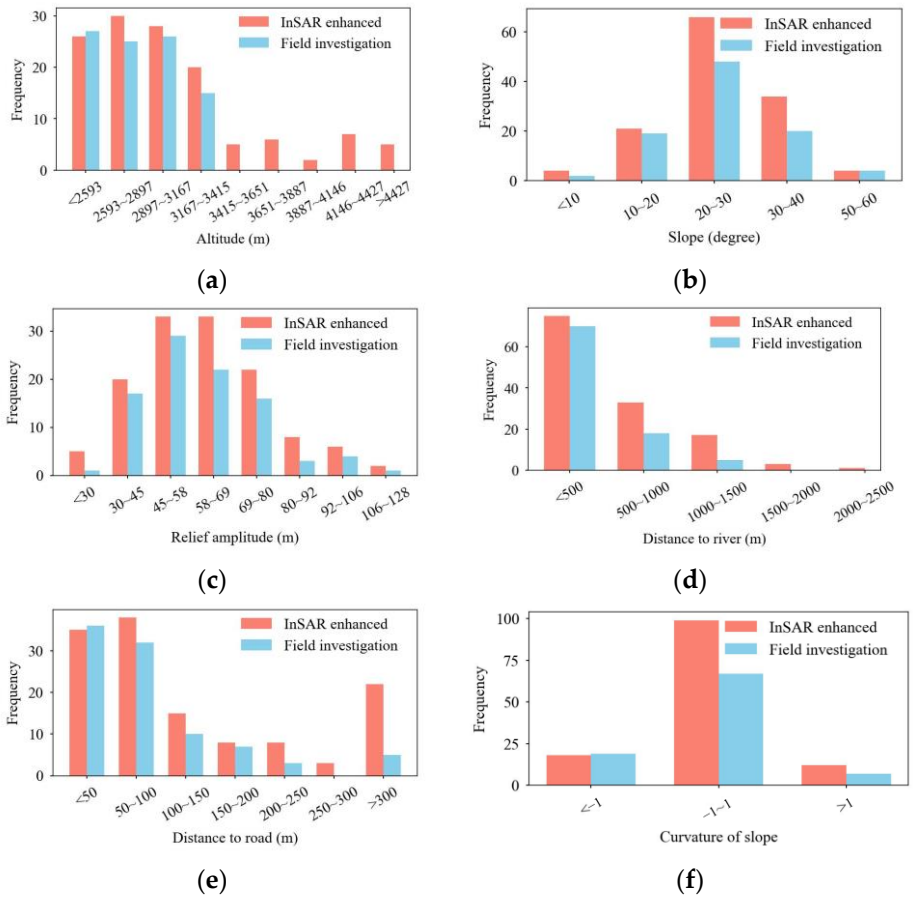


Figure 13. Histograms of landslides in the study area with respect to controlling factors of slope failure: (**a**) altitude, (**b**) slope, (**c**) relief amplitude, (**d**) distance to rivers, (**e**) distance to roads, and (**f**) curvature of slope. The red and blue bars represent the data sources of the InSAR analysis and field investigation, respectively.

Regarding the slope distribution, the slope angles of the landslides were mainly concentrated in the range 20°–30° in both the InSAR-enhanced and field investigation results (Figure 13b), indicating that this slope range controls the development of landslides in the study area. Although the slope angles of both data sets showed similar distribution patterns, clear differences could be observed in the slope angle ranges of 20°–30° and 30°–40°, with the InSAR results showing larger numbers of potential landslides by 37.5% and 70%, respectively. In this manner, the InSAR technique enhanced the identification of potential landslides in the slope angle ranges of 20°–30° and 30°–40° at the regional scale.

The relief amplitude refers to the maximum relative altitude difference within a certain distance in the landslide area, which was obtained through GIS analysis in this study. The search distance was set to be 100 m, which is the same as that in the analysis in Jiuzhaigou area by Yi et al. [74]. As shown in Figure 13c, the relief amplitude of the potential landslide sites obtained through the field investigation mainly fell in the range of 45–58 m, while the InSAR analysis revealed significant increases in potential landslides in every relief amplitude bin, especially in the range from 58 m to 92 m. The dominant relief amplitude extended from the range of 45–58 m to 45–69 m, implying that the relief amplitude from 45 to 69 m controls landslide development in the study area and more attention should be paid to this range in future risk assessment.

The distance to rivers is also a causative factor for landslide development as river water could erode the slope toe. Both the InSAR analysis and field investigation showed that landslide sites are mainly distributed within 500 m from rivers in the study area (Figure 13d) because toe erosion is more likely to occur at slopes close to the river. Moreover, the InSAR

analysis showed the occurrence of some landslides at a distance of greater than 1500 m from rivers. This indicates the possibility of other controlling factors in addition to river erosion in the study area. The detailed cause analysis of these landslides is beyond the scope of this study.

Figure 13e shows that the landslide sites are mainly located within a distance of 100 m from roads, indicating that road construction may be related to landslide development. When road constructions take place in mountainous areas, the slope cut generates free surfaces that essentially lead to the increase in the sliding force and the decrease in the anti-sliding force and cause potential landslides [10,75]. Furthermore, the InSAR analysis revealed 25 landslide sites in an area located more than 250 m away from the roads. This value is five times more than the counterpart in the existing landslide inventory and also implies that InSAR can detect potential landslides located in inaccessible areas that are difficult to identify through field surveys.

Slope curvature, as a controlling factor of landslide development, describes the shape of a slope. Positive and negative curvature values indicate upwardly convex and concave slope surfaces, respectively, while a value of 0 indicates a flat slope surface. Considering the error in measuring the topography, slopes with curvatures in the range of $[-1, 1]$ were considered as flat slopes in this study. The curvatures of the slopes from both data sets were analyzed, and the histograms are shown in Figure 13f. Both data sets indicated that most of the landslide sites developed on relatively flat slopes. Nevertheless, the InSAR analysis showed more landslides in the curvature range of $[-1, 1]$. This can be explained by the high-altitude difference of slopes in alpine regions, providing favorable conditions for material migration. With long-term weathering and erosion, the slope surface tends to be flattened, resulting in a small absolute value of curvature.

The abovementioned results suggest that the integration of InSAR with the analysis of landslide development significantly promotes deeper understanding of landslide causation factors such as altitude, distance to roads, and distance to rivers. In addition, the InSAR technique dramatically enhanced the dominant ranges of the factors of slope angle, relief amplitude, and curvature that determine the landslide development.

The development of landslides is also controlled by the geographical relationships between the slope aspect and the stratigraphic occurrence, major joints as well as wedges formed by the intersections of joint planes and strata bedding planes [76]. From the geological viewpoint, if the dip directions of the strata bedding planes and wedges are similar to the slope aspect, the area is prone to landslides because the strata bedding planes and joints could act as sliding surfaces due to their low shear strength. In this study, to show the influence of the InSAR analysis on the understanding of landslide development from a geological viewpoint, the stratigraphic occurrence, wedges, and slope aspect of landslide sites were statistically analyzed. As shown in the rose diagram in Figure 14a, the strata in this region mainly dip to the northeast and southwest because of the development of a series of NW-trending folds (Figure 3), and the wedges, which were determined by the kinematic analysis [76], predominantly dip to the west-northwest and east-southeast. The dip direction of strata and wedge indicate that slopes dipping towards these directions favor landslide development. Therefore, it is not surprising that a large number of landslides revealed by both field investigation (Figure 14b) and InSAR technique (Figure 14c) slide towards azimuths 270°–360° and 0°–135° that coincide well with the dip directions of the strata and wedges (Figure 14a). Furthermore, some landslides in the study area slide to 230°–270° (Figure 14b,c), which are beyond the dip direction ranges of the bedding planes and wedges. These landslides might not be controlled by the strata and wedges but by other mechanisms. For example, weathered materials slide along the soil–rock interface and/or the interfaces formed by complicated combinations of discontinuities. Even though the aspects of slopes in Figure 14b,c cover similar ranges, some difference still exist. To better highlight those differences, the rose diagram of the aspects of the newly identified landslides through the InSAR analysis is plotted in Figure 14d. The InSAR analysis not only enhanced the observation of landslides with similar aspects as

those in the field survey (e.g., 70°–130° and 230°–300°) but also revealed new landslides with aspects that are less predominant in the field survey (e.g., 10°–30° and 180°–210°). These newly identified landslides might be attributed to more complicated combinations of strata bedding planes and wedges that are difficult to identify in the field investigation. These observations suggest that the InSAR technique is powerful for identifying landslides in all dip directions and could improve the understanding on the significance of key factors controlling landslides at the regional scale, i.e., the stratigraphic occurrence and development of key joints in this study.

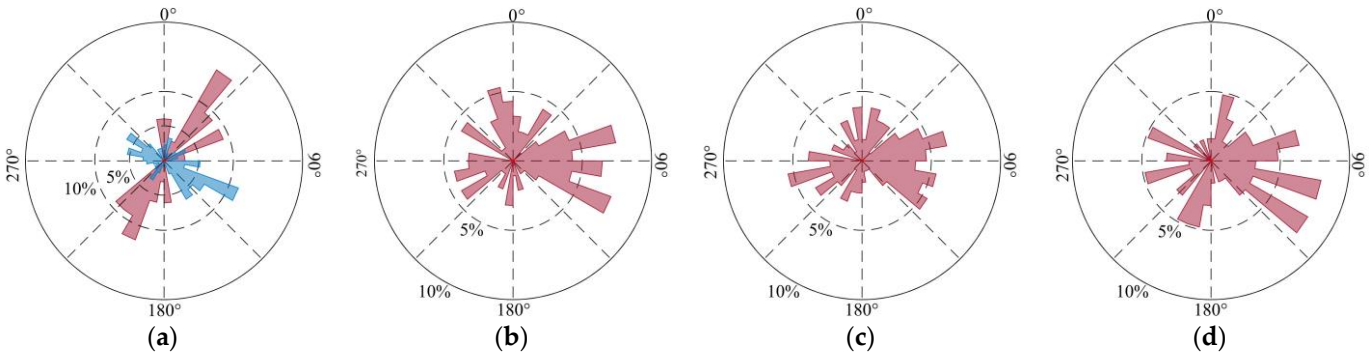


Figure 14. Rose diagrams of (**a**) the dip directions of the strata bedding planes (red) and wedges formed by the strata bedding planes and the key joints (blue) in the study area and the slope aspects of the landslide sites identified (**b**) in the field investigation, (**c**) by InSAR analysis, and (**d**) by InSAR analysis but not included in the field investigation.

The difference between the two data sets is attributed to the ability of InSAR to detect landslides on a regional scale. With this advantage, InSAR data can be used to analyze landslides over a wider spatial dimension, which is required for the correlation analysis between landslides and regional geological conditions. As shown in the rose diagrams of the slope aspects, landslides are not highly prominent along the strata dip direction but in the direction range of 70°–130° (Figure 14b,c), especially the landslides newly identified by the InSAR technique as being in the direction range of 105°–130° (Figure 14d). These directions indicate that the development of landslides could be affected by wedges. From a geological viewpoint, landslides controlled by wedges are relatively difficult to identify through field investigation due to the complicated combination of strata and joints. Nevertheless, by applying the large-scale InSAR analysis, the relationship between landslides and wedges could be more easily clarified.

In summary, the identification of potential landslides in alpine regions is a difficult task because of the high altitude and complicated terrain conditions. Objectively, if landslides do not exhibit clear deformation evidence or are located in inaccessible ridge-tops, they might not be identified in field investigation. Moreover, the frequency of field investigations is relatively low because of high costs and limitations of time and resources. Consequently, reactivated landslides (such as the TS2 landslide in Figure 6) are likely to be neglected, especially after intense rainfall events in summer. Such missed detection could lead to not only the underestimation of landslide risk in alpine areas but also an incomplete understanding of landslide development. For example, the relationships between altitude and landslide as well as the landslide controlled by complicated wedges in the study area cannot be fully clarified through field investigation. In contrast, SAR satellites feature wide spatial coverage and short revisit periods, enabling the detection of landslides in inaccessible areas and reactivated landslides. By incorporating newly identified landslides into the analysis of landslide development on a regional scale, the understanding of landslide development can be significantly improved. With the new landslide inventory and new information, the risk assessment in alpine regions can also be improved (Table 2). Therefore, when performing landslide risk assessment in alpine regions, a prior InSAR analysis is critical for obtaining precise results.

Table 2. Summary of findings in the current study.

Parameters	Landslide Inventory by Field Survey	Landslide Inventory by Field Survey and InSAR
Number of landslides	93	129
Altitude range	<3415 m	25 potential landslides at high altitudes >3415 m
Slope distribution	Mainly concentrated in 20°–30°	Mainly concentrated in 20°–30° but 37.5% and 70% increases in the ranges of 20°–30° and 30°–40°
Relief amplitude	Mainly concentrated in 45–58 m	Dominant relief amplitude expands to 45–69 m
Distance to rivers	Mainly distributed within 500 m	Some landslides at a distance of greater than 1500 m from rivers are observed
Distance to road	Mainly distributed within 100 m	25 landslide sites in an area located more than 250 m away from the roads
Slope curvature	Mainly located in [−1, 1]	Mainly located in [−1, 1]
Development pattern	Controlled by the strata and wedges	Not only controlled by the strata and wedges but also the combinations of strata bedding planes and wedges

5.2. Future Landslide Identification Using InSAR Techniques

In this study, a total of 81 landslides were identified in an area of 768.7 km^2 using only Sentinel-1 data, showing the high feasibility of InSAR analysis for landslide detection and enhancing the understanding of landslide development in the alpine forest region. As reported by previous studies, the performance of InSAR analysis, especially the deformation map, is influenced by the resolution of the SAR image. The higher the resolution of the SAR image, the more detailed the deformation characteristics of landslides that can be obtained. Thus, from the aspect of obtaining detailed landslide deformation characteristics, high-resolution SAR images are still required. With the development of remote sensing techniques, more commercial SAR satellites, such as COSMO-SkyMed and TerraSAR-X, have been launched to provide high-quality and high-resolution images. In future studies, such data sets can be adopted to perform integrated InSAR analyses with multi-resolution SAR images, which could provide more detailed deformation features as well as increase the detection rate [77,78]. In addition, the combination of both ascending and descending orbit data sets can overcome the poor observation induced by the shadow and foreshortening effects of SAR images to increase the detection ratio of potential landslides and, therefore, improve the identification of potential landslides. Therefore, the combination of multi-sensor data with different paths would also be helpful for observations in all azimuths [57]. For landslide detection with InSAR techniques in alpine forest regions, some key points need to be stressed in future studies. The temporal coherence of SAR images is a critical factor for obtaining precise ground deformation and identifying potential landslides [54] because it is significantly affected by the growth and withering of vegetation and snow and ice melting in alpine forest regions. In order to achieve higher temporal coherence, relatively longer wave length SAR data should be used. Although the C-band Sentinel-1 SAR data have already been shown to be feasible for landslide detection and providing new understanding on landslide development in this study, L-band sensors, such as ALOS-2, would be favorable for future landslide studies in alpine forest areas [79]. Another factor affecting the coherence of SAR images is the landslide itself. Fast-evolving landslides, such as the Baige landslides along the Jinsha River, are widely distributed in alpine forest regions, especially in the eastern area of the Tibetan Plateau, because of the steep terrain conditions and historical tectonic movement [80,81]. This type of landslide might not be detected through time-series analysis such as PS-InSAR and SBAS-InSAR because the coherence may not be sufficient [82]. Previous studies pointed out that traditional D-InSAR or Stacking-InSAR techniques are feasible tools for handling fast-evolving landslides [28]. Therefore, the combination of such InSAR techniques with time-series InSAR analysis can increase the detection ratio of potential landslides.

Another interesting phenomenon worth noting is that the boundaries of some potential landslide sites determined by the InSAR technique differ from those identified in the field investigations. This is because the InSAR technique and field investigation determine

the landslide boundaries using different methods. In field investigation, the boundaries are usually determined by the presence of distinct cracks or prior experience and might not be precise when this evidence is not sufficient on a slope. However, the InSAR technique determines the boundaries by differentiating areas with ground deformation from areas without deformation with high accuracy [83]. Therefore, the InSAR results provide more precise landslide boundaries in the satellite observation geometry [84]. It also should be clarified that the actual landslide boundary may not be the same as that determined by InSAR but should at least cover the deformation area, considering the geometric effects of SAR images. In other words, the landslide boundary should be the union set of the field investigation and InSAR results. Thus, in order to improve the accuracy of landslide boundary determination, one approach is to combine the InSAR results with field investigation and another is to apply multi-sensor data with different observing directions. In summary, InSAR techniques can significantly improve the results of field investigation for landslide identification. In future efforts on studies of potential landslides, improved results can be obtained by using multi-sensor and long-wavelength SAR data and combining InSAR results and field investigation.

6. Conclusions

Alpine forest regions, especially the eastern area of the Tibetan Plateau, are among the most landslide-prone areas owing to their complicated geological conditions and terrains. Understanding landslide development is a fundamental prerequisite for landslide susceptibility mapping and further landslide risk management. Incomplete landslide inventories may lead to underestimation of landslide risks and even lead to improper risk management strategies. Thus, for future landslide hazards risk management, a complete and precise landslide inventory is urgently required. However, in alpine forest regions, landslide identification through field surveying is a difficult and time-consuming task, and some landslides may not be detected. Thus, the current landslide inventory needs to be improved by incorporating objective and accurate observations. The InSAR technique is an efficient tool for this task owing to its ability to detect ground deformation with all-day and all-weather coverage. However, the role of the InSAR technique in understanding the development of potential landslides on the regional scale requires further clarification. Hence, aiming to promote the implementation of InSAR in landslide research in an alpine forest region, this study comparatively analyzed landslide inventories established using InSAR analysis and field investigation in Xiaojin County in the eastern area of the Tibetan Plateau. The results indicate that the InSAR technique is a feasible tool for identifying potential landslide sites as it can detect ground deformation with high accuracy and penetrate dense vegetation. It can not only improve the determination of the spatial distribution of landslides significantly but also contribute to the understanding of the historical deformation characteristics of landslides through continuous SAR observations. Moreover, InSAR analysis can not only facilitate the detection of the potential landslides but also provide deeper insight into landslide development at the regional scale. By establishing a complete landslide inventory using the InSAR technique, the understanding of landslide development with respect to the altitude, distance to roads, and distance to rivers is significantly improved at the regional scale. In addition, the joint analysis of InSAR results with geological conditions could improve understanding on the significance of the key factors controlling landslides at the regional scale, i.e., the stratigraphic occurrence and development of key joints. Therefore, when performing landslide risk assessment in alpine regions, a prior InSAR analysis is critical for obtaining a precise landslide inventory. For landslide identification, the InSAR analysis and field geological survey are complementary rather than competitive. On one hand, field geological surveys are more suitable for studying individual landslides and can provide detailed in situ landslide information, such as soil type, cracks, and failure mechanism. On the other hand, the InSAR analysis can be used to analyze landslides over a wider spatial dimension and to determine the regional development of landslides. Therefore, the combination of these two methods is of vital

importance for the understanding of the distribution and development of landslides at the regional scale.

Supplementary Materials: The following supporting information can be downloaded at: https://www.mdpi.com/article/10.3390/app132111851/s1. Table S1. Sentinel-1 data used for the SBAS-InSAR analysis. Figure S1. Spatial coverage of SAR data used in this study. Figure S2. Baseline connections of the SAR images used in this study for ascending (left) and descending (right) orbit data sets. The red dots indicate the super reference images.

Author Contributions: Conceptualization, S.Z. and Z.G.; methodology, S.Z.; software, S.Z.; validation, S.Z., Z.G., G.H. and K.L.; formal analysis, S.Z. and Z.G.; investigation, S.Z., G.H. and K.L.; resources, S.Z., G.H. and K.L.; data curation, S.Z., G.H. and K.L.; writing—original draft preparation, S.Z.; writing—review and editing, Z.G.; visualization, S.Z.; supervision, Z.G.; project administration, Z.G.; funding acquisition, Z.G. All authors have read and agreed to the published version of the manuscript.

Funding: This work is supported by the National Natural Science Foundation of China (Grant No. 42072301).

Data Availability Statement: The topographic data are available from the Earth Science Data Systems (ESDS) Program of NASA. The precipitation data in 1981–2010 in the study area are from the China Meteorological Data Service Center at http://data.cma.cn (accessed on 12 October 2023). The geological data in the study area are from the China Geological Survey at http://www.cgs.gov.cn/ (accessed on 12 October 2023). The SAR images are acquired from the European Space Agency (ESA). The STRMGL1 digital elevation model is downloaded from the Land Processes Distributed Active Archive Center (https://lpdaac.usgs.gov (accessed on 12 October 2023)). The Gaofen-2 optical images are collected from the China Center for Resources Satellite Date and Application (http://www.cresda.com/ (accessed on 12 October 2023)).

Acknowledgments: The InSAR analysis was performed using the open-source package InSAR Scientific Computing Environment version 2 (ISCE2, https://winsar.unavco.org/software/isce (accessed on 12 October 2023)). The SBAS analysis was performed with the Stanford Method for Persistent Scatterers (StaMPS, http://homepages.see.leeds.ac.uk/~earahoo/stamps/ (accessed on 12 October 2023)) software.

Conflicts of Interest: The authors declare no conflict of interest.

References

1. Turner, A.K. Social and environmental impacts of landslides. *Innov. Infrastruct. Solut.* **2018**, *3*, 70. [CrossRef]
2. van Westen, C.J.; van Asch, T.W.J.; Soeters, R. Landslide hazard and risk zonation—Why is it still so difficult? *Bull. Eng. Geol. Environ.* **2006**, *65*, 167–184. [CrossRef]
3. Guo, Z.; Zhou, M.; Huang, Y.; Pu, J.; Zhou, S.; Fu, B.; Aydin, A. Monitoring performance of slopes via ambient seismic noise recordings: Case study in a colluvium deposit. *Eng. Geol.* **2023**, *324*, 107268. [CrossRef]
4. Xu, C.; Xu, X.; Pourghasemi, H.R.; Pradhan, B.; Iqbal, J. Volume, gravitational potential energy reduction, and regional centroid position change in the wake of landslides triggered by the 14 April 2010 Yushu earthquake of China. *Arab. J. Geosci.* **2014**, *7*, 2129–2138. [CrossRef]
5. Yu, H.; Li, C.; Zhou, J.-Q.; Chen, W.; Long, J.; Wang, X.; Peng, T. Recent rainfall- and excavation-induced bedding rockslide occurring on 22 October 2018 along the Jian-En expressway, Hubei, China. *Landslides* **2020**, *17*, 2619–2629. [CrossRef]
6. Hearn, G.J. *Slope Engineering for Mountain Roads*; Geological Society of London: London, UK, 2011; ISBN 978-1-86239-331-8.
7. Hu, W.; Huang, R.; McSaveney, M.; Zhang, X.; Yao, L.; Shimamoto, T. Mineral changes quantify frictional heating during a large low-friction landslide. *Geology* **2018**, *46*, 223–226. [CrossRef]
8. Jerolmack, D.J.; Daniels, K.E. Viewing Earth's surface as a soft-matter landscape. *Nat. Rev. Phys.* **2019**, *1*, 716–730. [CrossRef]
9. Bontemps, N.; Lacroix, P.; Larose, E.; Jara, J.; Taipe, E. Rain and small earthquakes maintain a slow-moving landslide in a persistent critical state. *Nat. Commun.* **2020**, *11*, 780. [CrossRef] [PubMed]
10. Zhou, S.; Ouyang, C.; An, H.; Jiang, T.; Xu, Q. Comprehensive study of the Beijing Daanshan rockslide based on real-time videos, field investigations, and numerical modeling. *Landslides* **2020**, *17*, 1217–1231. [CrossRef]
11. Li, Q.; Wang, Y.M.; Zhang, K.B.; Yu, H.; Tao, Z.Y. Field investigation and numerical study of a siltstone slope instability induced by excavation and rainfall. *Landslides* **2020**, *17*, 1485–1499. [CrossRef]
12. Pradhan, S.; Toll, D.G.; Rosser, N.J.; Brain, M.J. An investigation of the combined effect of rainfall and road cut on landsliding. *Eng. Geol.* **2022**, *307*, 106787. [CrossRef]

13. Zhu, L.; Cui, S.; Pei, X.; Wang, S.; He, S.; Shi, X. Experimental investigation on the seismically induced cumulative damage and progressive deformation of the 2017 Xinmo landslide in China. *Landslides* **2021**, *18*, 1485–1498. [CrossRef]
14. Ma, K.; Zhang, Y.; Wu, H.; Ji, Z.; Ren, J.; Liang, Y.; Zhou, X. Shaking table test study of accumulation layer landslide under earthquake action. *Arab. J. Geosci.* **2022**, *15*, 161. [CrossRef]
15. Okura, Y.; Kitahara, H.; Ochiai, H.; Sammori, T.; Kawanami, A. Landslide fluidization process by flume experiments. *Eng. Geol.* **2002**, *66*, 65–78. [CrossRef]
16. Lee, K.; Suk, J.; Kim, H.; Jeong, S. Modeling of rainfall-induced landslides using a full-scale flume test. *Landslides* **2021**, *18*, 1153–1162. [CrossRef]
17. Zhang, Y.; Zhu, S.; Tan, J.; Li, L.; Yin, X. The influence of water level fluctuation on the stability of landslide in the Three Gorges Reservoir. *Arab. J. Geosci.* **2020**, *13*, 845. [CrossRef]
18. Das, P.; Patwa, D.; Bharat, T.V. Influencing factors on the simulation of rainfall-induced landslide prediction based on case study. *Bull. Eng. Geol. Environ.* **2022**, *81*, 194. [CrossRef]
19. Xie, W.; Guo, Q.; Wu, J.Y.; Li, P.; Yang, H.; Zhang, M. Analysis of loess landslide mechanism and numerical simulation stabilization on the Loess Plateau in Central China. *Nat. Hazards* **2021**, *106*, 805–827. [CrossRef]
20. Wu, J.; Zhang, Y.; Yang, L.; Zhang, Y.; Lei, J.; Zhi, M.; Ma, G. Identifying the essential influencing factors of landslide susceptibility models based on hybrid-optimized machine learning with different grid resolutions: A case of Sino-Pakistani Karakorum Highway. *Environ. Sci. Pollut. Res.* **2023**, *30*, 100675–100700. [CrossRef]
21. Domakinis, C.; Oikonomidis, D.; Astaras, T. Landslide mapping in the coastal area between the Strymonic Gulf and Kavala (Macedonia, Greece) with the aid of remote sensing and geographical information systems. *Int. J. Remote Sens.* **2008**, *29*, 6893–6915. [CrossRef]
22. Li, Y.; Xiao, J.; Cong, N.; Yu, X.; Lin, Y.; Liu, T.; Qi, G.; Ren, P. Modeling Ecological Resilience of Alpine Forest under Climate Change in Western Sichuan. *Forests* **2023**, *14*, 1769. [CrossRef]
23. Wang, Y.; Liu, D.; Dong, J.; Zhang, L.; Guo, J.; Liao, M.; Gong, J. On the applicability of satellite SAR interferometry to landslide hazards detection in hilly areas: A case study of Shuicheng, Guizhou in Southwest China. *Landslides* **2021**, *18*, 2609–2619. [CrossRef]
24. Song, C.; Yu, C.; Li, Z.; Pazzi, V.; Del Soldato, M.; Cruz, A.; Utili, S. Landslide geometry and activity in Villa de la Independencia (Bolivia) revealed by InSAR and seismic noise measurements. *Landslides* **2021**, *18*, 2721–2737. [CrossRef]
25. Zhang, Y.; Li, D.; Yin, K.; Chen, L.; Xu, Y.; Woldai, T.; Lian, Z. The July 1, 2017 Wangjiawan landslide in Ningxiang County, China. *Landslides* **2018**, *15*, 1657–1662. [CrossRef]
26. Bayer, B.; Simoni, A.; Mulas, M.; Corsini, A.; Schmidt, D. Deformation responses of slow moving landslides to seasonal rainfall in the Northern Apennines, measured by InSAR. *Geomorphology* **2018**, *308*, 293–306. [CrossRef]
27. Moretto, S.; Bozzano, F.; Mazzanti, P. The Role of Satellite InSAR for Landslide Forecasting: Limitations and Openings. *Remote Sens.* **2021**, *13*, 3735. [CrossRef]
28. Zhang, L.; Dai, K.; Deng, J.; Ge, D.; Liang, R.; Li, W.; Xu, Q. Identifying Potential Landslides by Stacking-InSAR in Southwestern China and Its Performance Comparison with SBAS-InSAR. *Remote Sens.* **2021**, *13*, 3662. [CrossRef]
29. Ouyang, C.; Zhao, W.; He, S.; Wang, D.; Zhou, S.; An, H.; Wang, Z.; Cheng, D. Numerical modeling and dynamic analysis of the 2017 Xinmo landslide in Maoxian County, China. *J. Mt. Sci.* **2017**, *14*, 1701–1711. [CrossRef]
30. Zhao, S.; Chigira, M.; Wu, X. Buckling deformations at the 2017 Xinmo landslide site and nearby slopes, Maoxian, Sichuan, China. *Eng. Geol.* **2018**, *246*, 187–197. [CrossRef]
31. Intrieri, E.; Raspini, F.; Fumagalli, A.; Lu, P.; Del Conte, S.; Farina, P.; Allievi, J.; Ferretti, A.; Casagli, N. The Maoxian landslide as seen from space: Detecting precursors of failure with Sentinel-1 data. *Landslides* **2018**, *15*, 123–133. [CrossRef]
32. Xie, M.; Zhao, W.; Ju, N.; He, C.; Huang, H.; Cui, Q. Landslide evolution assessment based on InSAR and real-time monitoring of a large reactivated landslide, Wenchuan, China. *Eng. Geol.* **2020**, *277*, 105781. [CrossRef]
33. Liu, X.; Zhao, C.; Zhang, Q.; Lu, Z.; Li, Z.; Yang, C.; Zhu, W.; Liu-Zeng, J.; Chen, L.; Liu, C. Integration of Sentinel-1 and ALOS/PALSAR-2 SAR datasets for mapping active landslides along the Jinsha River corridor, China. *Eng. Geol.* **2021**, *284*, 106033. [CrossRef]
34. Hu, C.; Chen, Z.; Li, Y.; Dong, X.; Hobbs, S. Research progress on geosynchronous synthetic aperture radar. *Fundam. Res.* **2021**, *1*, 346–363. [CrossRef]
35. Xie, M.; Huang, J.; Wang, L.; Huang, J.; Wang, Z. Early landslide detection based on D-InSAR technique at the Wudongde hydropower reservoir. *Environ. Earth Sci.* **2016**, *75*, 717. [CrossRef]
36. Wang, G.; Xie, M.; Chai, X.; Wang, L.; Dong, C. D-InSAR-based landslide location and monitoring at Wudongde hydropower reservoir in China. *Environ. Earth Sci.* **2013**, *69*, 2763–2777. [CrossRef]
37. Kiseleva, E.; Mikhailov, V.; Smolyaninova, E.; Dmitriev, P.; Golubev, V.; Timoshkina, E.; Hooper, A.; Samiei-Esfahany, S.; Hanssen, R. PS-InSAR Monitoring of Landslide Activity in the Black Sea Coast of the Caucasus. *Procedia Technol.* **2014**, *16*, 404–413. [CrossRef]
38. Rosi, A.; Tofani, V.; Tanteri, L.; Tacconi Stefanelli, C.; Agostini, A.; Catani, F.; Casagli, N. The new landslide inventory of Tuscany (Italy) updated with PS-InSAR: Geomorphological features and landslide distribution. *Landslides* **2018**, *15*, 5–19. [CrossRef]
39. Yalvac, S. Validating InSAR-SBAS results by means of different GNSS analysis techniques in medium- and high-grade deformation areas. *Environ. Monit. Assess.* **2020**, *192*, 120. [CrossRef]

40. Zhang, J.; Gao, B.; Huang, H.; Chen, L.; Li, Y.; Yang, D. SBAS-InSAR-Based Landslide Susceptibility Mapping Along the North Lancang River, Tibetan Plateau. *Front. Earth Sci.* **2022**, *10*, 901889. [CrossRef]
41. Hilley, G.E.; Bürgmann, R.; Ferretti, A.; Novali, F.; Rocca, F. Dynamics of Slow-Moving Landslides from Permanent Scatterer Analysis. *Science* **2004**, *304*, 1952–1955. [CrossRef]
42. Murray, K.D.; Lohman, R.B.; Kim, J.; Holt, W.E. An Alternative Approach for Constraining 3D-Displacements With InSAR, Applied to a Fault-Bounded Groundwater Entrainment Field in California. *J. Geophys. Res. Solid Earth* **2021**, *126*, e2020JB021137. [CrossRef]
43. Bianchini, S.; Cigna, F.; Righini, G.; Proietti, C.; Casagli, N. Landslide HotSpot Mapping by means of Persistent Scatterer Interferometry. *Environ. Earth Sci.* **2012**, *67*, 1155–1172. [CrossRef]
44. Zhou, C.; Cao, Y.; Yin, K.; Wang, Y.; Shi, X.; Catani, F.; Ahmed, B. Landslide Characterization Applying Sentinel-1 Images and InSAR Technique: The Muyubao Landslide in the Three Gorges Reservoir Area, China. *Remote Sens.* **2020**, *12*, 3385. [CrossRef]
45. Bouchra, A.; Mustapha, H.; Mohammed, R. D-InSAR Analysis of Sentinel-1 Data for Landslide Detection in Northern Morocco, Case Study: Chefchaouen. *J. Geosci. Environ. Prot.* **2020**, *8*, 84–103. [CrossRef]
46. Liu, Y.; Qiu, H.; Yang, D.; Liu, Z.; Ma, S.; Pei, Y.; Zhang, J.; Tang, B. Deformation responses of landslides to seasonal rainfall based on InSAR and wavelet analysis. *Landslides* **2022**, *19*, 199–210. [CrossRef]
47. Ouyang, C.; Zhao, W.; An, H.; Zhou, S.; Wang, D.; Xu, Q.; Li, W.; Peng, D. Early identification and dynamic processes of ridge-top rockslides: Implications from the Su Village landslide in Suichang County, Zhejiang Province, China. *Landslides* **2019**, *16*, 799–813. [CrossRef]
48. Chang, M.; Sun, W.; Xu, H.; Tang, L. Identification and deformation analysis of potential landslides after the Jiuzhaigou earthquake by SBAS-InSAR. *Environ. Sci. Pollut. Res.* **2023**, *30*, 39093–39106. [CrossRef]
49. Xu, Q.; Guo, C.; Dong, X.; Li, W.; Lu, H.; Fu, H.; Liu, X. Mapping and Characterizing Displacements of Landslides with InSAR and Airborne LiDAR Technologies: A Case Study of Danba County, Southwest China. *Remote Sens.* **2021**, *13*, 4234. [CrossRef]
50. Li, S.; Xu, W.; Li, Z. Review of the SBAS InSAR Time-series algorithms, applications, and challenges. *Geod. Geodyn.* **2022**, *13*, 114–126. [CrossRef]
51. Peng, T.; Chen, Y.; Chen, W. Landslide Susceptibility Modeling Using Remote Sensing Data and Random SubSpace-Based Functional Tree Classifier. *Remote Sens.* **2022**, *14*, 4803. [CrossRef]
52. Wang, N.; Cheng, W.; Wang, B.; Liu, Q.; Zhou, C. Geomorphological regionalization theory system and division methodology of China. *J. Geogr. Sci.* **2020**, *30*, 212–232. [CrossRef]
53. Xie, W.; Li, X.; Jian, W.; Yang, Y.; Liu, H.; Robledo, L.F.; Nie, W. A Novel Hybrid Method for Landslide Susceptibility Mapping-Based GeoDetector and Machine Learning Cluster: A Case of Xiaojin County, China. *ISPRS Int. J. Geo-Inf.* **2021**, *10*, 93. [CrossRef]
54. Hooper, A.; Zebker, H.; Segall, P.; Kampes, B. A new method for measuring deformation on volcanoes and other natural terrains using InSAR persistent scatterers. *Geophys. Res. Lett.* **2004**, *31*. [CrossRef]
55. Hooper, A.; Segall, P.; Zebker, H. Persistent scatterer interferometric synthetic aperture radar for crustal deformation analysis, with application to Volcán Alcedo, Galápagos. *J. Geophys. Res. Solid Earth* **2007**, *112*. [CrossRef]
56. Hooper, A. A multi-temporal InSAR method incorporating both persistent scatterer and small baseline approaches. *Geophys. Res. Lett.* **2008**, *35*. [CrossRef]
57. Luo, X.; Wang, C.; Long, Y.; Yi, Z. Analysis of the Decadal Kinematic Characteristics of the Daguangbao Landslide Using Multi-platform Time Series InSAR Observations After the Wenchuan Earthquake. *J. Geophys. Res. Solid Earth* **2020**, *125*, e2019JB019325. [CrossRef]
58. Berardino, P.; Fornaro, G.; Lanari, R.; Sansosti, E. A new algorithm for surface deformation monitoring based on small baseline differential SAR interferograms. *IEEE Trans. Geosci. Remote Sens.* **2002**, *40*, 2375–2383. [CrossRef]
59. Cigna, F.; Esquivel Ramírez, R.; Tapete, D. Accuracy of Sentinel-1 PSI and SBAS InSAR Displacement Velocities against GNSS and Geodetic Leveling Monitoring Data. *Remote Sens.* **2021**, *13*, 4800. [CrossRef]
60. Hooper, A.; Bekaert, D.; Spaans, K.; Arıkan, M. Recent advances in SAR interferometry time series analysis for measuring crustal deformation. *Tectonophysics* **2012**, *514*, 1–13. [CrossRef]
61. Hooper, A. A Statistical-Cost Approach to Unwrapping the Phase of InSAR Time Series. In Proceedings of the International Workshop on ERS SAR Interferometry, Frascati, Italy, 30 November 2010.
62. Zhou, S.; Ouyang, C.; Huang, Y. An InSAR and depth-integrated coupled model for potential landslide hazard assessment. *Acta Geotech.* **2022**, *17*, 3613–3632. [CrossRef]
63. Herrera, G.; Gutiérrez, F.; García-Davalillo, J.C.; Guerrero, J.; Notti, D.; Galve, J.P.; Fernández-Merodo, J.A.; Cooksley, G. Multi-sensor advanced DInSAR monitoring of very slow landslides: The Tena Valley case study (Central Spanish Pyrenees). *Remote Sens. Environ.* **2013**, *128*, 31–43. [CrossRef]
64. Lu, P.; Casagli, N.; Catani, F.; Tofani, V. Persistent Scatterers Interferometry Hotspot and Cluster Analysis (PSI-HCA) for detection of extremely slow-moving landslides. *Int. J. Remote Sens.* **2012**, *33*, 466–489. [CrossRef]
65. Getis, A.; Ord, J.K. The Analysis of Spatial Association by Use of Distance Statistics. *Geogr. Anal.* **1992**, *24*, 189–206. [CrossRef]
66. Ord, J.K.; Getis, A. Local Spatial Autocorrelation Statistics: Distributional Issues and an Application. *Geogr. Anal.* **1995**, *27*, 286–306. [CrossRef]

67. Ren, T.; Gong, W.; Gao, L.; Zhao, F.; Cheng, Z. An Interpretation Approach of Ascending–Descending SAR Data for Landslide Identification. *Remote Sens.* **2022**, *14*, 1299. [CrossRef]
68. Meisina, C.; Zucca, F.; Notti, D.; Colombo, A.; Cucchi, A.; Savio, G.; Giannico, C.; Bianchi, M. Geological Interpretation of PSInSAR Data at Regional Scale. *Sensors* **2008**, *8*, 7469–7492. [CrossRef]
69. Rose, N.D.; Hungr, O. Forecasting potential rock slope failure in open pit mines using the inverse-velocity method. *Int. J. Rock Mech. Min. Sci.* **2007**, *44*, 308–320. [CrossRef]
70. van Westen, C.J.; Castellanos, E.; Kuriakose, S.L. Spatial data for landslide susceptibility, hazard, and vulnerability assessment: An overview. *Eng. Geol.* **2008**, *102*, 112–131. [CrossRef]
71. Ouyang, C.; An, H.; Zhou, S.; Wang, Z.; Su, P.; Wang, D.; Cheng, D.; She, J. Insights from the failure and dynamic characteristics of two sequential landslides at Baige village along the Jinsha River, China. *Landslides* **2019**, *16*, 1397–1414. [CrossRef]
72. Dai, K.; Xu, Q.; Li, Z.; Tomás, R.; Fan, X.; Dong, X.; Li, W.; Zhou, Z.; Gou, J.; Ran, P. Post-disaster assessment of 2017 catastrophic Xinmo landslide (China) by spaceborne SAR interferometry. *Landslides* **2019**, *16*, 1189–1199. [CrossRef]
73. Liu, X.; Zhao, C.; Zhang, Q.; Lu, Z.; Li, Z. Deformation of the Baige Landslide, Tibet, China, Revealed Through the Integration of Cross-Platform ALOS/PALSAR-1 and ALOS/PALSAR-2 SAR Observations. *Geophys. Res. Lett.* **2020**, *47*, e2019GL086142. [CrossRef]
74. Yi, Y.; Zhang, Z.; Zhang, W.; Jia, H.; Zhang, J. Landslide susceptibility mapping using multiscale sampling strategy and convolutional neural network: A case study in Jiuzhaigou region. *CATENA* **2020**, *195*, 104851. [CrossRef]
75. Lin, F.; Wu, L.Z.; Huang, R.Q.; Zhang, H. Formation and characteristics of the Xiaoba landslide in Fuquan, Guizhou, China. *Landslides* **2018**, *15*, 669–681. [CrossRef]
76. Goodman, R.E. *Introduction to Rock Mechanics*, 2nd ed.; Wiley: New York, NY, USA, 1991; ISBN 978-0-471-81200-5.
77. Bovenga, F.; Wasowski, J.; Nitti, D.O.; Nutricato, R.; Chiaradia, M.T. Using COSMO/SkyMed X-band and ENVISAT C-band SAR interferometry for landslides analysis. *Remote Sens. Environ.* **2012**, *119*, 272–285. [CrossRef]
78. Du, Y.; Xu, Q.; Zhang, L.; Feng, G.; Li, Z.; Chen, R.-F.; Lin, C.-W. Recent Landslide Movement in Tsaoling, Taiwan Tracked by TerraSAR-X/TanDEM-X DEM Time Series. *Remote Sens.* **2017**, *9*, 353. [CrossRef]
79. Tantianuparp, P.; Shi, X.; Zhang, L.; Balz, T.; Liao, M. Characterization of Landslide Deformations in Three Gorges Area Using Multiple InSAR Data Stacks. *Remote Sens.* **2013**, *5*, 2704–2719. [CrossRef]
80. Fan, X.; Xu, Q.; Alonso-Rodriguez, A.; Subramanian, S.S.; Li, W.; Zheng, G.; Dong, X.; Huang, R. Successive landsliding and damming of the Jinsha River in eastern Tibet, China: Prime investigation, early warning, and emergency response. *Landslides* **2019**, *16*, 1003–1020. [CrossRef]
81. Xiong, Z.; Feng, G.; Feng, Z.; Miao, L.; Wang, Y.; Yang, D.; Luo, S. Pre- and post-failure spatial-temporal deformation pattern of the Baige landslide retrieved from multiple radar and optical satellite images. *Eng. Geol.* **2020**, *279*, 105880. [CrossRef]
82. Zhang, S.; Yin, Y.; Hu, X.; Wang, W.; Zhang, N.; Zhu, S.; Wang, L. Dynamics and emplacement mechanisms of the successive Baige landslides on the Upper Reaches of the Jinsha River, China. *Eng. Geol.* **2020**, *278*, 105819. [CrossRef]
83. Intrieri, E.; Frodella, W.; Raspini, F.; Bardi, F.; Tofani, V. Using Satellite Interferometry to Infer Landslide Sliding Surface Depth and Geometry. *Remote Sens.* **2020**, *12*, 1462. [CrossRef]
84. Dai, K.; Li, Z.; Tomás, R.; Liu, G.; Yu, B.; Wang, X.; Cheng, H.; Chen, J.; Stockamp, J. Monitoring activity at the Daguangbao mega-landslide (China) using Sentinel-1 TOPS time series interferometry. *Remote Sens. Environ.* **2016**, *186*, 501–513. [CrossRef]

Disclaimer/Publisher's Note: The statements, opinions and data contained in all publications are solely those of the individual author(s) and contributor(s) and not of MDPI and/or the editor(s). MDPI and/or the editor(s) disclaim responsibility for any injury to people or property resulting from any ideas, methods, instructions or products referred to in the content.